

To appear in ApJ Letters.

## Shaping point- and mirror-symmetric proto-planetary nebulae by the orbital motion of the central binary system

Sinhué A. R. Haro-Corzo, Pablo F. Velázquez, Alejandro C. Raga

*Instituto de Ciencias Nucleares, Universidad Nacional Autónoma de México, Ciudad Universitaria, Apartado Postal 70-543, CP 04510, México D.F., México.*

haro,pablo,raga@nucleares.unam.mx

Angels Riera

*Departament de Física i Enginyeria Nuclear, EUETIB, Universitat Politècnica de Catalunya, Comte d'Urgell 187, E-08036 Barcelona, Spain.*

*Departament d'Astronomia i Meteorologia, Universitat de Barcelona, Av. Diagonal 647, 08028 Barcelona, Spain.*

*Institut d'Estudis Espacials de Catalunya (IEEC), E-08034 Barcelona, Spain.*

Primož Kajdic

*Instituto de Geofísica, Universidad Nacional Autónoma de México, Ciudad Universitaria, México D.F., México.*

### ABSTRACT

We present 3D hydrodynamical simulations of a jet launched from the secondary star of a binary system inside a proto-planetary nebula. The secondary star moves around the primary in a close eccentric orbit. From the gasdynamic simulations we compute synthetic  $[\text{N II}] \lambda 6583$  emission maps. Different jet axis inclinations with respect to the orbital plane, as well as different orientations of the flow with respect to the observer are considered. For some parameter combinations, we obtain structures that show point- or mirror-symmetric morphologies depending on the orientation of the flow with respect to the observer. Furthermore, our models can explain some of the emission distribution asymmetries that are summarized in the classification given by Soker & Hadar (2002).

*Subject headings:* ISM: jets and outflows — planetary nebulae: general — stars: AGB and post-AGB — methods: numerical — binaries: general

## 1. Introduction

The shell of ionized gas coming from the ejected envelopes of the very late stage in the death of an intermediate initial mass ( $M_* \leq 8 M_\odot$ ) star is called Planetary Nebula (PN). Since the onset of high spatial resolution observational facilities, such as the HST, optical images of PNe have revealed a rich variety of morphologies, highly collimated structures and small scale features. These nebulae have been classified according to their large-scale morphologies as: bipolar, circular, elliptical or irregular. In particular, bipolar PNe are axially symmetric, having two lobes with an equatorial waist between them.

Soker & Hadar (2002) proposed a classification of PNe depending on their departure from axisymmetry. The departures from axial symmetry can be point-symmetry or mirror-symmetry, with respect to the equatorial plane (which separates the two lobes).

In the last decade, the point-symmetric shape of some PNe and proto-planetary nebulae (PPNe) has been successfully explained in terms of collimated outflows. For example, Lee & Sahai (2003) carried out axisymmetrical simulations for modeling the morphology and emission of the PPN CRL 618. Velázquez et al. (2004) (also see Riera et al. 2004), modeled the multiple shocked structures, emission and kinematics of the PPN Hen 3-1475 in terms of a precessing jet with a periodic velocity variation, using 3D hydrodynamical simulations. Velázquez et al. (2007) modeled the thermal radio-continuum emission of the PN K3-35 as a continuous, precessing jet. Guerrero et al. (2008) present an observational and numerical study of the PN IC 4634, showing that a variable velocity, precessing jet is the origin of its point-symmetric morphology. Some features observed in PNe (i.e. low excitation knots/clumps moving at supersonic velocities) could be produced by cosmic “bullets” (e.g., Raga et al. 2007; Dennis et al. 2008).

The presence of a companion to the AGB star is thought to be required in order to produce jets and point-symmetric morphologies (Balick & Frank 2002). The presence of binary star system progenitors of PNe was initially proposed by Bond et al. (1978), who discovered that UU Sge, the central star of PN Abell 63, is an eclipsing binary. Fabian & Hansen (1979) suggested that the particular shape of the Helix nebula can also be due to the action of a binary system. Livio et al. (1979) suggested that non-spherical PNe host close binaries. Furthermore, the survey of De Marco et al. (2008) shows strong evidence that at least 10-15% of PNe are composed of binary systems with short orbital periods ( $< 3$  days). Eventhough this fraction is not high enough to be consistent with the large fraction of PNe that apparently have been shaped by binary interactions, this survey is not able to detect large orbital periods and therefore the binary fraction of 10-15% has been considered a lower limit.

Some mechanism invoked to explain the shaping of bipolar PNe involve the action of jets

launched by the primary or secondary star (e.g., Morris 1987, 1990; Soker 1992; Livio 1993; Soker & Rappaport 2000). In several models, the jets are supposed to form when a main sequence star (or a white dwarf) accrete material from the AGB (or post-AGB) star, forms an accretion disk and blows two jets (e.g., Frank & Blackman 2004; Frank 2006; Frank et al. 2007). Hydrodynamical simulations have shown that jets (blown by the AGB star or by a companion) can account for some of the observed morphologies. García-Arredondo & Frank (2004) carried out 3D numerical simulations of the interaction of the stellar winds from the components of a binary system. They found that bipolar morphologies as narrow-waisted nebulae can be obtained after the interaction of a slow AGB wind, from the primary star, with a collimated fast stellar wind produced by the secondary.

In this work, we explore the influence of having a binary system in order to reproduce the morphology and brightness distribution of bipolar PPNe. We investigate (3D hydrodynamical simulations) if both point- and mirror- symmetric PPN could be explained in terms of an interacting jet (source in orbital motion) with an AGB wind. Also, we explore if the observed morphology of the PPN is affected by the orientation of the flow with respect to the observer. The jet is ejected by the secondary star (a star in the main sequence), which is on orbital motion around the remnant of the AGB star. For simplicity, the AGB wind is considered isotropic, i.e., it has a density distribution given by  $\rho_w \propto r^{-2}$  and a constant wind velocity (see section 3). We consider a close eccentric binary system, calling the suggestions of Soker et al. (1998), Soker & Rappaport (2000) and Soker & Rappaport (2001).

## 2. Modeling the orbital motion of a binary system

We investigate the interaction of a jet with the AGB slow wind in a binary system scenario, where the primary is the remnant AGB star. Observations show that many PNe seem to have binary sources (van Winckel 2003; Zijlstra 2007; De Marco et al. 2008), in which the two stars can be in different evolutionary stages according to their initial masses.

Both stars orbit around the center of mass in stable elliptical paths. The Keplerian velocity of the reduced mass is corrected by the factor  $M_p/(M_s + M_p)$ , in order to obtain the orbital velocity of the secondary star. The orbital plane (the  $xy$ - plane) is such that both foci of the ellipse are located along the  $x$ -axis, i.e. both the periastron and apoastron lie along this axis. With this configuration, the orbital velocity achieves its maximum magnitude in the periastron, toward the positive  $y$ -axis (see panel (a) of Figure 1).

van Winckel (2003) gives values for the semi-major axis of the order of 1 AU, while PNe usually have physical sizes of  $\sim 0.1$  pc ( $\sim 10^5$  AU). As we are interested in modeling

the large scale structure of PNe, the spatial resolution of our numerical simulations is not high enough to resolve the scale of the orbital motion. However, our numerical simulations do resolve the temporal scale of the Keplerian motion, so that we can include the orbital speed as an additional component of the outflow velocity. In panels (b) and (c) of Figure 1, we display the actual scheme used, i.e. a fixed jet, centered in the computational domain, where the orbital speed is added to the jet velocity. Two snapshots are shown for the cases where the orbital speed is maximum –at the periastron, panel (b)– and minimum –at the apoastron, panel (c)–.

A detailed exploration of the parameter space (semi-major axis, eccentricity, etc) is carried out by Haro-Corzo et al. (2009, in preparation). In this work, we only show the most relevant results, choosing  $M_p + M_s = 1.25 M_\odot$  (with  $M_p = 1M_\odot$ ) and a semi-major axis of 3.2 AU (i.e., an orbital period of 5 years).

### 3. Initial setup for the numerical simulations

The 3D numerical simulations were carried out with the YGUAZÚ-A code (Raga et al. 2000). The YGUAZÚ-A code integrates the gas-dynamical equations together with a system of rate equations for the atomic/ionic species: HI, HII, HeI, HeII, HeIII, CII, CIII, CIV, NI, NII, NIII, OI, OII, OIII, OIV, SII and SIII. With these rate equations, a non-equilibrium cooling function is computed. The reaction and cooling rates are described in detail by Raga et al. (2002). The gas-dynamical equations are integrated with a second order accurate technique (in time and space) employing the “flux-vector splitting” algorithm of van Leer (1982).

Our numerical simulations use a 5-level, binary, adaptive Cartesian grid, in a computational domain of  $256 \times 256 \times 512$  pixels (at the highest grid resolution) along the  $x$ -,  $y$ -, and  $z$ - axes. The size of the computational domain is of  $2 \times 10^{17}$  cm along the  $x$ - and  $y$ -directions, and  $4 \times 10^{17}$  cm along the  $z$ -direction.

A jet is injected into a circumstellar medium, which has been swept up previously by a dense and slow wind from the AGB central star. Even though the circumstellar medium in bipolar PNe is aspherical (with higher densities in the equator than along the bipolar axis), for simplicity and in order to only study the influence of the binary orbital motion, we have “turned off” the AGB influence imposing on all computational domain the analytical solution of an isotropic AGB wind. Then, the wind density distribution is given by:

$$\rho_w = \frac{\dot{M}_w}{4 \pi r^2 v_w}, \quad (1)$$

where  $\dot{M}_w$  is the mass loss rate of the AGB wind,  $v_w$  is the AGB wind terminal velocity, and  $r$  is the distance from the primary star. We assume that the AGB wind is initially neutral, with  $\dot{M}_w = 2 \times 10^{-6} M_\odot \text{ yr}^{-1}$ ,  $v_w = 1.5 \times 10^6 \text{ cm s}^{-1}$  and a temperature  $T_w = 100 \text{ K}$ . A decreasing temperature vs. radius dependence (resulting from the adiabatic expansion of the spherically diverging wind) is generated as the time-integration progresses.

The jet is injected at the center of the computational domain within a cylindrical volume with radius  $r_j$  and length  $l_j$  with values  $r_j = l_j = 4 \times 10^{15} \text{ cm}$ . (which are equivalent to 5 pixels in the highest resolution grid). The jet temperature was set to  $10^3 \text{ K}$ . The jet velocity is  $v_j = 1.7 \times 10^7 \text{ cm s}^{-1}$  and the mean atom + ion number density is constant with  $n_j = 5 \times 10^4 \text{ cm}^{-3}$ . These values correspond to a  $\dot{M}_j = 1.5 \times 10^{-6} M_\odot \text{ yr}^{-1}$  mass injection, which could seem high. Due to the limited numerical resolution we are forced to impose the jet on a region larger than its true size. However, the total injected mass after 400 yr is  $1.2 \times 10^{-3} M_\odot$ , which looks like reasonable (Velázquez et al. 2007).

With the parameters listed above, the jet is in the domain of “strong jet” according to the description of Soker & Rappaport (2000) and García-Arredondo & Frank (2004), with a parameter  $\chi = \dot{M}_w v_w / \dot{M}_j v_j = 0.2$ . A similar dynamical behaviour could be achieved taking into account a less dense jet but with higher velocity, keeping constant the jet ram pressure  $\rho_j v_j^2$  and the parameter  $\chi$ . However, we prefer to employ a dense jet with a low velocity, being the last one comparable with the maximum orbital speed, in order to favor the contribution of orbital motion to the global morphology of the object. Based in these initial conditions, we consider six runs labeled as *Rai* and *Rbi*, where  $i=1$  corresponds to the case in which the jet axis is perpendicular to the orbital plane,  $i=2$  to a tilt of  $20^\circ$  between the jet axis and the orbital axis, on the  $xz$ -plane, and  $i=3$  to a tilt of  $20^\circ$  on the  $yz$ -plane (the orbital axis is parallel to the  $z$ -axis, and the  $x$ -axis contains the foci of the elliptical orbit, see §2). Runs *Rai* have an eccentricity  $e = 0.73$ , and runs *Rbi* have  $e = 0.94$ . The parameters of the runs are summarized in Table 1.

Finally, from the temperature and atomic/ionic/electronic number density distributions computed from the numerical time-integration, we calculate the emission line coefficients of a set of permitted and forbidden emission lines. The forbidden line  $[\text{N II}] \lambda 6583$  was computed by solving 5-level atom problems, using the parameters of Mendoza (1983).

## 4. Results

We find that many of our jet/AGB wind interaction models have morphologies that depend on the projection, and that both point- and mirror- symmetric PNe can be obtained

from the same model (depending on the position of the observer). This is illustrated in Figure 2, where we plot the resulting synthetic [N II]  $\lambda$  6583 emission maps at an integration time of 400 yr. The group of six panels correspond to the runs *Rai*. The  $yz$ - and  $xz$ -projections of run *Ra1* show mirror-symmetric morphology. On the other hand, while the  $yz$ - projection of run *Ra2* has a mirror-symmetric morphology, the  $xz$ -projection of this model has a point-symmetric morphology. A similar switch between point- and mirror-symmetric morphologies is seen in run *Ra3*. Also, we analyze the asymmetries of the synthetic [N II]  $\lambda$  6583 emission maps for runs *Rai* produced by the inclination ( $40^\circ$ ) of the orbital plane ( $xz$ -plane) with respect to the plane of the sky. The intensity maps preserve the mirror- and point-symmetric morphologies discussed above (for the case in which the  $z$ -axis lies on the plane of the sky). Furthermore, we find that the morphologies of the maps obtained from runs *Rbi* are similar to the maps from *Rai*, although in general, we note the presence of small-scale internal structures which are brighter for runs *Rbi* than runs *Rai*. Those are because of the larger eccentricity of the *Rbi* runs. The velocity variability of the jet (resulting from the orbital motion), produces these internal substructures in both lobes of the *Rai* and *Rbi* maps. In order to see the influence of the increasing eccentricity, in the figure 3 we display the subtraction of the synthetic [N II]  $\lambda$  6583 emission maps corresponding to *Rbi*- *Rai* runs.

Finally, we have obtained the [N II]  $\lambda$  6583 luminosities for the top and bottom lobes for all of the computed maps. Table 2 gives the [N II]  $\lambda$  6583 luminosities for both lobes and all runs. In general, we note that runs *Rbi* have larger [N II]  $\lambda$  6583 luminosities than runs *Rai* (of the order of a 10%), as a result of the more eccentric orbital motion of runs *Rbi*. The exception is the run *Rb3* because the total luminosity measured on the top lobe is the same of run *Ra3*, while the bottom lobe has less total luminosity. This is due to the gas material of top lobe has larger velocities than the bottom lobe gas. In the top lobe, the orbital motion speed is added to the jet velocity, while the opposite occurs for the bottom lobe. For the cases where the resulting shape has mirror-symmetry, the luminosities from the right and left sides of the lobes have also been computed. Comparison of total luminosities between both (top and bottom) lobes show a similar value for runs *Ra1*, *Ra2*, *Rb1* and *Rb2*. However, analyzing the  $xz$ - and  $yz$ - projection cases, an asymmetry in the brightness distribution is observed for the  $yz$ -projection, in general, with the right side being more luminous, consequence of the orbital motion. In runs *Ra3* and *Rb3* we obtain appreciable [N II]  $\lambda$  6583 luminosity asymmetries between the top and bottom lobes (see figure 3).

Point- and mirror-symmetric morphologies are simultaneously obtained if the jet axis has a certain inclination with respect to the orbital plane. Interestingly, the classification of a PN belonging to one or other group seems to depend on the point of view of the observer or on the projection. There are significant differences in the total luminosities of both lobes between runs *Ra2* and *Ra3* and similar behavior is observed for runs *Rb2* and *Rb3*. Run

*Rb2* produces top and bottom lobes with similar total luminosities, while run *Rb3* generates a luminosity difference of at least 36% between the top and bottom lobes. This is due to the fact that the jet axis is tilted  $20^\circ$  on the  $yz$ -plane in the case of run *Ra3*. In this case, the jet inclination contributes to the elliptical motion, being its effect larger for the top lobe when the secondary star passes by the periastron, where the orbital motion velocity is maximum. The total jet velocity (the intrinsic constant jet velocity  $\sim 1.7 \times 10^7 \text{ cm s}^{-1}$  plus the eccentric orbital motion velocity) is also maximum at the periastron, producing strong shocks and increasing the emission for the top lobe (the opposite occurs for the bottom lobe).

## 5. Discussion and Conclusions

In this work, we carried out 3D hydrodynamical simulations with the YGUAZÚ-A code in order to explore the binarity mechanism for shaping bipolar, point- and mirror-symmetric PN. We consider a collimated outflow (jet) launched by the secondary star of a binary system, located at the center of a PN. The primary star is the source of the AGB wind, in which the jet is embedded. The two stars have a close, very eccentric orbit, resulting in a maximum orbital velocity of the order of the jet velocity. Because of this, the orbital velocity has a strong effect on the jet dynamics, and strongly modifies the emission line maps predicted from the computed flows.

We have generated [N II]  $\lambda 6583$  emission maps considering different inclinations of the jet axis with respect to the orbital plane and also different tilts between the orbital axis and the line of sight. We find that the predicted maps of some runs exhibit (see figure 2) either point- or mirror-symmetric substructures depending on the orientation of the flow with respect to the observer. Also, the maps exhibit substructures with different luminosities for the two lobes and with side-to-side asymmetries within the same lobe.

In this sense, Soker & Hadar (2002) built a classification of PNe based on their departure from axisymmetry considering both morphological and brightness distribution criteria. From Figure 2 and table 2, we note that runs *Ra3* and *Rb3* would correspond to class 2 (i.e. unequal intensity of both sides) of Soker & Hadar (2002), because top lobes are brighter than bottom ones. Into this class could be also included maps of runs *Ra1* and *Ra2*, for example, because in their  $yz$ -projection display an asymmetry in the right and left brightness distribution. The  $yz$ -projections of *Ra1* and *Rb1* could be also included in the class 4 (i.e. the jets are bent to the same side, therefore there is a mirror-symmetry), because the small-scale structure observed on the right side of both lobes.

From our study we conclude that a jet ejected from a companion to the AGB star

(which gives rise to a PN) in a highly eccentric orbit leads to morphologies with either point- or mirror-symmetries (in some cases both, depending on the inclination to the observer). Also, the bipolar nebular structure resulting from the jet/AGB stellar wind interaction has brightness asymmetries with contrasts similar to the asymmetries observed in some PNe (Soker & Hadar 2002). We must note that, except for the eccentricity, the orbital parameters we used are commonly found in last evolution state of low mass and small post-AGB stars, which can be a close binaries without a common envelope (van Winckel 2003; Frankowski 2004; Van Winckel et al. 2009; de Marco 2009). The eccentricities we used are uncommon for post-AGB stars, however, there are reports of highly eccentric orbits in other binary systems, such as Ba stars (van Winckel 2003; Jorissen et al. 1998). de Marco (2009) argued that for post-AGB stars that have been monitored spectroscopically, low eccentricities have been found for systems with intermediate periods (between 100 to 1500 days), but for periods  $> 1$  yr the eccentricities can be close to unity). A larger sample of post-AGB in binary systems is needed to assess the feasibility of our model.

It is interesting that we can generate models which produce either point- or mirror-symmetric emission line maps, depending only on the orientation of the flow with respect to the observer. For other choices of flow parameters, however, it is easy to obtain models which produce point-symmetric structures regardless of the orientation of the flow with respect to the observer (e. g., by having a precessing jet from a source with low orbital velocity, Masciadri & Raga 2002). Therefore, while a large range of parameters will produce point-symmetric nebulae, we find that it is necessary to have both an appropriate parameter combination and an appropriate orientation of the flow (with respect to the observer) in order to produce mirror-symmetric structures. This result might be consistent with the fact that many more bipolar PNe are observed to have point-symmetric structures (as opposed to mirror-symmetric structures). In order to decide whether this is indeed the case, a more detailed study limiting the parameter space relevant for nebulae resulting from jet/AGB wind interactions will have to be made, as well as a study of the statistics of the resulting flow morphologies observed at random orientations.

Authors acknowledge anonymous referee for her/his very useful comments and suggestions. We thank Martín Guerrero and Luis F. Miranda for many clarifying and useful comments. The authors acknowledge support from grants, CONACyT 46828-F, and DGAPA IN119709. The work of A.R. was supported by the MICINN grant AYA2008-06189-C03 and AYA2008-04211-C02-01 (co-funded with FEDER funds). We also thank Enrique Palacios, Antonio Ramírez and Martín Cruz for the assistance provided, and Alejandro Esquivel for reading this manuscript.

## REFERENCES

- Balick, B., & Frank, A. 2002, *ARA&A*, 40, 439
- Bond, H. E., Liller, W., & Mannery, E. J. 1978, *ApJ*, 223, 252
- de Marco, O. 2009, *PASP*, 121, 316, 0902.1137
- De Marco, O., Hillwig, T. C., & Smith, A. J. 2008, *ArXiv e-prints*, 804, 0804.2436
- Dennis, T. J., Cunningham, A. J., Frank, A., Balick, B., Blackman, E. G., & Mitran, S. 2008, *ApJ*, 679, 1327
- Fabian, A. C., & Hansen, C. J. 1979, *MNRAS*, 187, 283
- Frank, A. 2006, in *IAU Symposium, Vol. 234, Planetary Nebulae in our Galaxy and Beyond*, ed. M. J. Barlow & R. H. Méndez, 293–296
- Frank, A., & Blackman, E. G. 2004, *ApJ*, 614, 737
- Frank, A., De Marco, O., Blackman, E., & Balick, B. 2007, *ArXiv e-prints*, 0712.2004
- Frankowski, A. 2004, in *Astronomical Society of the Pacific Conference Series, Vol. 313, Asymmetrical Planetary Nebulae III: Winds, Structure and the Thunderbird*, ed. M. Meixner, J. H. Kastner, B. Balick, & N. Soker, 511–+
- García-Arredondo, F., & Frank, A. 2004, *ApJ*, 600, 992
- Guerrero, M. A. et al. 2008, *ApJ*, 683, 272, 0804.1812
- Haro-Corzo, S., Velazquez, P., & et al. 2009, in preparation
- Jorissen, A., Van Eck, S., Mayor, M., & Udry, S. 1998, *A&A*, 332, 877, [arXiv:astro-ph/9801272](https://arxiv.org/abs/astro-ph/9801272)
- Lee, C.-F., & Sahai, R. 2003, *ApJ*, 586, 319
- Livio, M. 1993, in *IAU Symposium, Vol. 155, Planetary Nebulae*, ed. R. Weinberger & A. Acker, 279–+
- Livio, M., Salzman, J., & Shaviv, G. 1979, *MNRAS*, 188, 1
- Masciadri, E., & Raga, A. C. 2002, *ApJ*, 568, 733
- Mendoza, C. 1983, *IAUS*, 103, 143

- Morris, M. 1987, *PASP*, 99, 1115
- Morris, M. 1990, in *From Miras to Planetary Nebulae: Which Path for Stellar Evolution?*, ed. M. O. Mennessier & A. Omont, 520–535
- Raga, A. C., de Gouveia Dal Pino, E. M., Noriega-Crespo, A., Mininni, P. D., & Velázquez, P. F. 2002, *A&A*, 392, 267
- Raga, A. C., Esquivel, A., Riera, A., & Velázquez, P. F. 2007, *ApJ*, 668, 310
- Raga, A. C., Navarro-González, R., & Villagrán-Muniz, M. 2000, *Revista Mexicana de Astronomía y Astrofísica*, 36, 67
- Riera, A., Velázquez, P. F., & Raga, A. C. 2004, in *Astronomical Society of the Pacific Conference Series*, Vol. 313, *Asymmetrical Planetary Nebulae III: Winds, Structure and the Thunderbird*, ed. M. Meixner, J. H. Kastner, B. Balick, & N. Soker, 487
- Soker, N. 1992, *ApJ*, 389, 628
- Soker, N., & Hadar, R. 2002, *MNRAS*, 331, 731
- Soker, N., & Rappaport, S. 2000, *ApJ*, 538, 241
- . 2001, *ApJ*, 557, 256
- Soker, N., Rappaport, S., & Harpaz, A. 1998, *ApJ*, 496, 842
- van Leer, B. 1982, in *Lecture Notes in Physics*, Berlin Springer Verlag, Vol. 170, *Numerical Methods in Fluid Dynamics*, ed. E. Krause, 507–512
- van Winckel, H. 2003, *ARA&A*, 41, 391
- Van Winckel, H. et al. 2009, *ArXiv e-prints*, 0906.4482
- Velázquez, P. F., Gómez, Y., Esquivel, A., & Raga, A. C. 2007, *MNRAS*, 382, 1965
- Velázquez, P. F., Riera, A., & Raga, A. C. 2004, *A&A*, 419, 991, [arXiv:astro-ph/0403126](https://arxiv.org/abs/astro-ph/0403126)
- Zijlstra, A. A. 2007, *Baltic Astronomy*, 16, 79

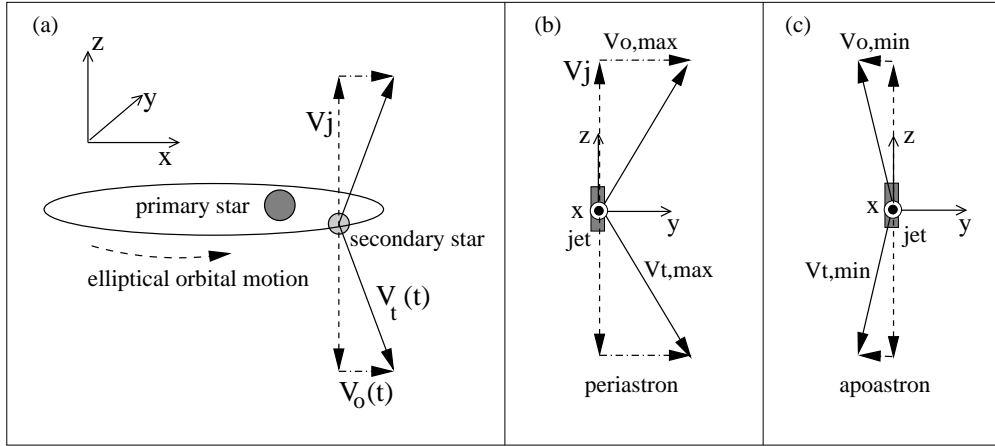


Fig. 1.— (a) Scheme of a vertical jet in orbital motion. The center of mass is located in one focus of an elliptical orbit and the secondary star orbits in an elliptical path around the center of mass (which lies close to the primary star). The foci are along the  $x$ -axis. The  $xy$ -plane is the orbital plane. (b) and (c) are the true scheme employed in our simulations, where the jet is located at the origin. The orbital speed is added as an additional component of the jet outflow.

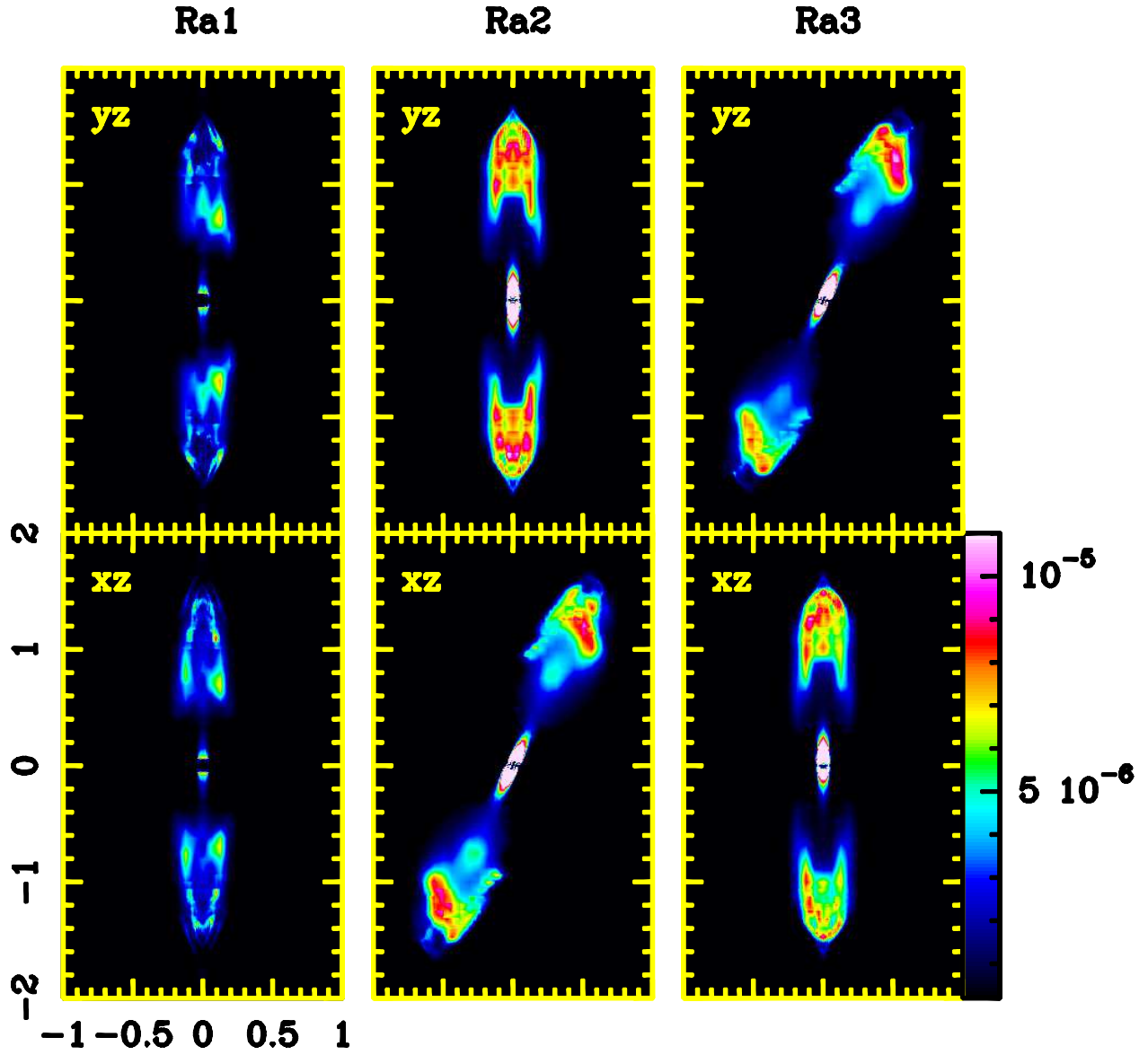


Fig. 2.— Synthetic [N II]  $\lambda 6583$  emission ( $\text{erg s}^{-1} \text{cm}^{-2} \text{sr}^{-1}$ ) at 400 yr for runs *Ra1*, *Ra2* and *Ra3*. The emission is on log gray-scale. Axes are in units of  $10^{17}$  cm. [See electronic edition for a color version.]

Table 1: Run parameters.

run	ecc	angle( $^{\circ}$ )	plane
Ra1	0.73	0	-
Ra2	0.73	20	xz
Ra3	0.73	20	yz
Rb1	0.94	0	-
Rb2	0.94	20	xz
Rb3	0.94	20	yz

Table 2: Luminosity of top and bottom lobes  $L/L_{\odot}(10^{-5})$ . Each lobe has been parted as left and right side. We ignore the central emission (20 pixels from each lobe).

Run	Bottom	xz		yz		Top	xz		yz	
	total	left	right	left	right	total	left	right	left	right
Ra1	3.4	1.7	1.7	1.3	2.1	3.4	1.7	1.7	1.3	2.1
Ra2	6.9	-	-	3.2	3.7	6.9	-	-	3.2	3.7
Ra3	5.6	2.9	2.7	-	-	6.9	3.6	3.3	-	-
Rb1	3.8	1.9	1.9	1.5	2.3	3.7	1.8	1.9	1.5	2.2
Rb2	7.6	-	-	3.4	4.2	7.4	-	-	3.3	4.1
Rb3	5.	2.6	2.4	-	-	6.8	3.6	3.2	-	-

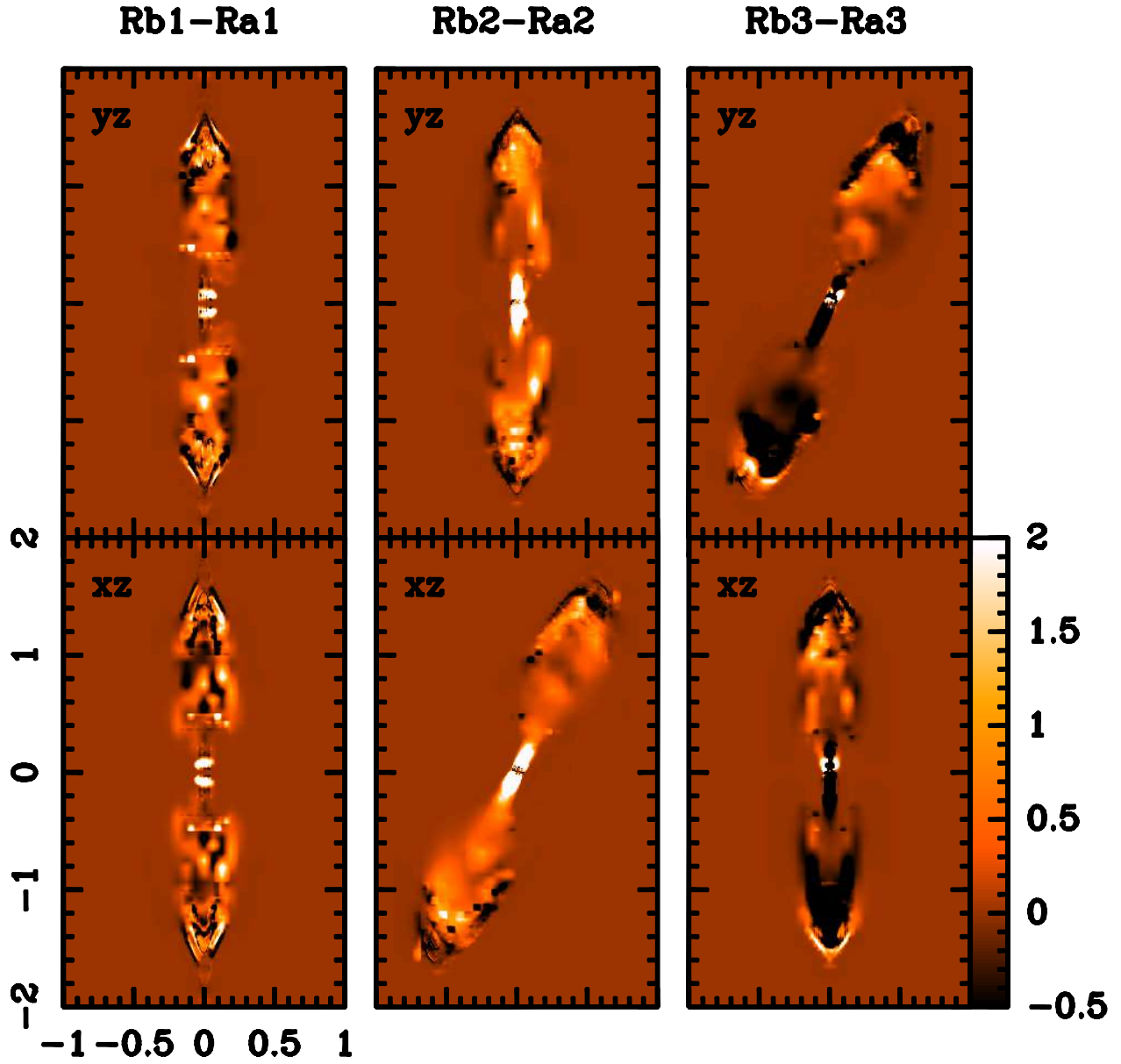


Fig. 3.— Synthetic [N II]  $\lambda$  6583 emission at 400 yr. for the subtraction  $Rb_i - Rai$ . Same scale as figure 2. [See electronic edition for a color version.]